Chapter 5

Impulsive Origin of Spicule-like Jets in the Solar Atmosphere

In this chapter, using observations of the coronal hole in Si IV 1393.755 Å line obtained with Interface Region Imaging Spectrograph (IRIS) on 8th October 2013, we revealed non-Gaussian line profiles presenting unusual line broadening that correspond to the plasma velocity enhancement. We have revisited the analysis of Chen et al. (2019) to find out a case of velocity enhancement that is linked to the formation of a cool spicule-like jet. This observational scenario may be caused by the localized impulsive energy release associated with the footpoint of the spicule-like cool jet. We analyze a specific event showing non-Gaussian profiles in the Si IV 1393.755 Å line, for a lifetime of 3.0 min and Doppler shifts reaching 68 kms^{-1}***, which is associated with a spicule-like jet of length 8.0 Mm. We model this jet by implementing an observed velocity enhancement in a magnetized, gravitationally-stratified, two dimensional (2-D) model solar atmosphere. The model atmosphere consists of open magnetic fields and realistic temperature profile. The velocity perturbation of ≈68*** kms^{-1}***, resembling the***

observed velocity enhancement, launches a thin spicule-like jet whose properties closely match with the observed jet. We also show that non-adiabatic conditions (e.g., thermal-conduction and radiative-cooling) affect the jet propagation, mass-flux, and kinetic energy density. We demonstrate that such spicule-like jets may transport mass and energy into the overlying solar atmosphere. The synthetic images derived from the use of simulation data (e.g., density, temperature) and atomic parameters of Si IV 1393.755 Å from CHIANTI database, show that model jet consists of bright plasma as detected in the emissions at transition region (TR) temperature. It also consists of a cool core material that indicates its origin in the solar chromosphere. This cool chromospheric material appears as a dark plasma thread seen in the synthetic images that is eventually not evident in the Si IV emissions. IRIS Si IV emissions capture the heated counterpart of the observed jet, which is also evident in the synthetic images as a bright feature. Complementing the recent observations revealing the impulsive origin of the spicule-like jets, our present model emphasizes comprehensively their evolution in both adiabatic and non-adiabatic conditions of the solar atmosphere. The model implicitly displays the presence of the hot and cool components of jet's plasma. It also demonstrates that the cooling atmosphere affects the kinematics and energetics of the jets. This work is published in "The European Physical Journal Plus".

A.K. Srivastava, Balveer Singh, K. Murawski, Y. Chen, K. Sharma, D. Yuan, S.K. Tiwari, M. Mathioudakis: *The European Physical Journal Plus, 138, 209 (2023)*

5.1 Introduction

The quiet solar chromosphere is having complex magnetic field structuring, which provides a portal for the evolution of cool jets at diverse spatio-temporal scales (e.g., spicules, macrospicules, tornadoes, network jets, surges etc) (e.g., De Pontieu et al., 2011, 2004; Kayshap et al., 2013a,b; Kuridze et al., 2015; Martínez-Sykora et al., 2017a; Panesar et al., 2019, 2020; Reid et al., 2016; Samanta et al., 2019; Shibata et al., 2007; Srivastava et al., 2018; Tian et al., 2014; Uddin et al., 2012; Wang et al., 2021; Wedemeyer-Böhm et al., 2012, and references cited therein). The spicules are the most spectacular recurrent plasma ejecta triggered in the entire lower solar atmosphere to transport the mass and energy to the overlying corona and nascent solar wind (e.g., De Pontieu et al., 2004, 2021; Kuźma et al., 2017b; Pereira et al., 2014; Samanta et al., 2019; Sterling, 2000; Wójcik et al., 2019; Zhang et al., 2012, and references cited therein). Recently, the high-resolution chromospheric observations from space and ground demonstrate the existence of spicule-like thin and cool jets in various parts of the solar atmosphere whose properties are similar to the typical spicules, however, they possess a variety of additional dynamical, and heating properties (e.g., Morton, 2012; Pereira et al., 2014; Shetye et al., 2016; Srivastava et al., 2017, 2018; Tian et al., 2014; Tsiropoula et al., 2012, and references cited therein). In the recent years, there are several attempts to understand new morphological appearances and physical properties of such spicule-like jets (e.g., formation of knots; bright bulky heads; high apparent speeds; fine structures; additional heating, etc) using various theoretical and numerical modelings (e.g. Cranmer and Woolsey, 2015; Kuźma et al., 2017b; Mackenzie Dover et al., 2021; Srivastava et al., 2018, and references cited therein). Traditionally apart from the typical spicules, the longer macrospicules are also observed and modeled in the solar atmosphere, which may have impulsive origin (e.g., Bennett and Erdélyi, 2015; González-Avilés et al., 2021; Murawski et al., 2011; Wilhelm, 2000). Recently, the thin jet-like structures, initially found in IRIS coronal hole (CH) observations, were observed

and termed as the network jets essentially as a transition region plasma processes (e.g., Tian et al., 2014).

The network jets associated with their footpoint brightening, show an apparent terminal speed of ≈80-250 km s^{-1}, lifetime 20-158 s, length 4-10 Mm, and average width of ≈ 300 km (e.g., Kayshap et al., 2018; Tian et al., 2014). On the contrary to the previous findings, Kayshap et al. (2018) reported an important physical property of QS network jets that they may exhibit rotational motion with a mean velocity of 49.56 kms^{-1}. The morphological feature, length, lifetime and speed of the network jets show some resemblance to the spicules, and it is possible that spicules or spicule-like cool jets may further be heated to TR temperatures (Pereira et al., 2014). Therefore, the latest cohort of the space and ground-based observations show the presence of various sub-classes of chromospheric jets that possess a range of morphological, plasma, and dynamical properties (e.g., De Pontieu et al., 2021; Kayshap et al., 2018; Pereira et al., 2014; Rast et al., 2021; Wedemeyer-Böhm et al., 2012; Zhang et al., 2012, and references cited therein). Qi et al. (2019) studied the relation between plumes and network jets. They found that network regions associated with stronger coronal plumes, which are more denser and brighter structures, produce dynamical network jets. Chen et al. (2019) also observed the signature of impulsive energy release, possibly associated with typical explosive events (EEs) at subarcsecond scales. They recorded the strong non-Gaussian profiles and blue- and red-shifted velocities of up to 150 kms^{-1} in Si IV 1402.8 Å, Mg II k 2796.4 Å and C II 1334.5 Å lines. These most possible impulsive energy release may even be associated with the small-scale plasma ejections, however, they do not fall in the realm of previously discovered network jets (e.g., Kayshap et al., 2018; Tian et al., 2014). Such impulsive events have also been observed as unusual broadening in the Si IV 1402.8 Å line (up to 200 kms^{-1}), and lead to the formation of a flowing cool loop system (e.g., Huang et al., 2015; Rao et al., 2019; Srivastava et al., 2020). The observational clues that emerged over the past few years demonstrate that the upper

chromospheric/TR velocity enhancements are ubiquitous in quiet-Sun, coronal holes, and in the vicinity of solar active regions, which subsequently generate the plasma flows (e.g., Chen et al., 2019; Huang et al., 2014, 2015, 2020; Srivastava et al., 2020). The localized plasma flows, driven by the impulsive energy release in the solar chromosphere/TR, can transport mass and momentum to the overlying atmosphere and may also contribute to the nascent solar wind (Rao et al., 2019). Recently, Chintzoglou et al. (2018) have found that spicular material may suspend high in the solar atmosphere but at lower temperatures as seen in Ly-α. It can be visible in TR temperatures in form of network jets where heating occurs lower in the spicule and further propagates upwards as a rapidly propagating thermal front.

Chen et al. (2019) observed double peaked Si IV 1393.755 Å line profiles or enhancements in both the line wings at network lanes, which are associated with the footpoints of network jets or transient compact quiet-Sun brightening. They elucidated that these broadened Si line profiles may be formed due to the occurrence of reconnection generated explosive events (EEs). The important scientific clues came in to picture when Chen et al. (2019) found a relation between unusual broadening of Si IV line profiles and its connection with the possible impulsive energy release, and subsequent formation of the cool chromospheric jets. They termed these observed jets as the network jets. The observational results given by Chen et al. (2019), however, did not establish the entire kinematics of those cool jets except their association with the locations related to the unusual line-broadening and velocity enhancement. Such impulsive velocity enhancements may also trigger a variety of chromospheric jets (e.g., spicules, marcospicules, network jets, etc), collectively termed as cool spicule-like jets.

In general the chromospheric jets are well collimated plasma ejecta at diverse spatio-temporal scales (e.g., spicules, macrospicules, network jets, etc) that may transport mass and energy into the overlying solar atmosphere. At many instances, the rotation/helical

twist is evident in some of the samples of these observed jets, e.g., associated with swirls/tornadoes, network jets, macrospicules (e.g., De Pontieu et al., 2021; Kamio et al., 2010; Kayshap et al., 2018; Liu et al., 2019; Rast et al., 2021; Wedemeyer-Böhm et al., 2012, references cited there). The reconnection based jet models invoke quite satisfactorily the episodic jet motions which are associated with the twisting or helical motions of their spire (Pariat et al., 2015). As far as newly discovered network jets and macrospicules are concerned, there are less information available on their triggering mechanisms. The most likely scenario of their trigger is found to be associated with impulsive energy release and associated plasma perturbations/flows. Yang et al. (2018b) have reported a numerical model based on the magnetic reconnection. In this model, the reconnection is driven by a combination of magnetic flux emergence and horizontal advection, which trigger both network jets and spicules in the solar atmosphere simultaneously. The small-scale, localized reconnection may yield some energy burst in the lower solar atmosphere, which can indirectly influence the stable plasma environment to further lead to the collimated plasma motions in form of the chromospheric jets. This classical scenario of jet formation is not associated directly with the Lorentz force as studied by many authors (e.g., Iijima and Yokoyama, 2017; Martínez-Sykora et al., 2017a; Nishizuka et al., 2008, and references cited therein). On the contrary to this particular scenario, it depicts the onset of plasma pressure or velocity perturbations at photospheric/chromospheric heights and thus evolution of the shock-enabled plasma ejecta as an aftermath of localized heating or transfer of momentum (e.g., Kayshap et al., 2013b; Mackenzie Dover et al., 2021; Martínez-Sykora et al., 2009; Murawski et al., 2011; Shibata et al., 1982; Singh et al., 2019; Srivastava et al., 2018, and references cited therein). In particular for the chromospheric small-scale jets, there are several modeling works related to the impulsive energy release (e.g., EEs/blinkers in TR; reconnection generated heating and transport of momentum, etc) that demonstrate physically how these jets are produced due to the magnetic reconnection (e.g., Ding

et al., 2011; Innes et al., 2015; Roussev et al., 2001a,b, and references cited therein). Some of these studies have already demonstrated that energy deposition from magnetic reconnection in various parts of the solar atmosphere triggers plasma upflows, which in turn can produce jet-like motions in an open magnetic-field configuration. The physical properties of the modeled jet may vary depending on the initial boundary conditions of the numerical simulations. The Alfvén waves are also proposed to trigger the chromospheric spicules in the solar atmosphere (e.g., Hollweg, 1982; Kudoh and Shibata, 1999; Singh et al., 2022, and references cited there). The production of the spicules were also envisaged when ion-neutral collisions damped the high-frequency Alfvén waves in the lower solar atmosphere (James et al., 2003). The strong amplitude Alfvénic oscillations are also observed in spicules to power them (De Pontieu et al., 2007b; Martínez-Sykora et al., 2017a; McIntosh et al., 2011; Srivastava et al., 2021a, 2017).

Apart from above mentioned developments, there are several recent attempts to model the two-fluid or multi-fluid descriptions of the solar chromosphere, which undergoes into wave-like or impulsive perturbations in the presence of ion and neutrals, and generate a variety of wave motions, small-scale plasma motions (e.g., spicules, cool jets), and localized shocks/pseudo-shocks (e.g., Martínez-Sykora et al., 2017b, 2020; Srivastava et al., 2018; Wójcik et al., 2019; Zhang et al., 2021, and references cited therein). There are a multitude of two fluid and multi-fluid models about waves and reconnection processes, which are significant in explaining chromospheric/coronal heating and generation of the dynamical plasma processes (e.g., Khomenko and Collados, 2012; Khomenko et al., 2018; Khomenko, 2017; Kuridze et al., 2015; Kuźma et al., 2017b; Popescu Braileanu et al., 2019; Soler et al., 2013b, and references cited there). The first self-consistent multi-fluid simulations of chromospheric magnetic reconnection in a weakly ionized reacting plasma was devised by Leake et al. (2012). Their numerical simulations provide signature that magnetic reconnection in the partially ionized chromosphere could be accountable for the

jet-like transients, e.g., spicules and other cool chromospheric jets. The flux emergence and magnetic reconnection in the solar chromosphere can generate the heating, shock, and jet-like motions (e.g., Hillier et al., 2016; Khomenko, 2017; Ni et al., 2015, 2016, 2018; Takasao et al., 2013). Many transient energy release processes (e.g., Ellerman bombs (EBs), UV bursts) and associated plasma dynamics in the lower solar atmosphere have been studied extensively under the framework of 3-D radiative magnetohydrodynamic (MHD) simulations (e.g., Hansteen et al., 2019; Hong et al., 2021; Ni et al., 2020, and references cited there). Many of these models consist of non-ideal terms such as conduction, cooling, and radiation, as well as wave dissipation by ion-neutral collisions, thus giving a pivotal information about the heating and dynamics of the chromospheric plasma (e.g., Ballester et al., 2018; González-Morales et al., 2020; Kuźma et al., 2021; Wójcik et al., 2020, and references cited there).

In this chapter, we revisit a single explosive event presented in Chen et al. (2019), which we model in the frame-work of magnetohydrodynamics (MHD) using PLUTO code. Section 5.2 consists of the details of observational results. An MHD model of the jet associated with the velocity enhancement in the localized solar atmosphere, is described in the Section 5.3. In the Section 5.4, we describe about the perturbations. In the Section 5.5, we briefly discuss about the numerical methods. Numerical results are presented in Section 5.6. The last section outlines the discussion and conclusions.

5.2 Observations

IRIS performed a large sit-and-stare observation (120″ along the slit) of a coronal hole boundary region during 19:56 – 23:26 UT on 2013 October 8. The pointing coordinates were (249″, 283″) and the roll angle of 90 degrees relative to the North South axis. The spatial resolution of the spectral and slit-jaw images (SJIs) was ≈0.167″ per pixel. The sit-and-stare spectral observation had a cadence of ~32 s, while the average cadence of

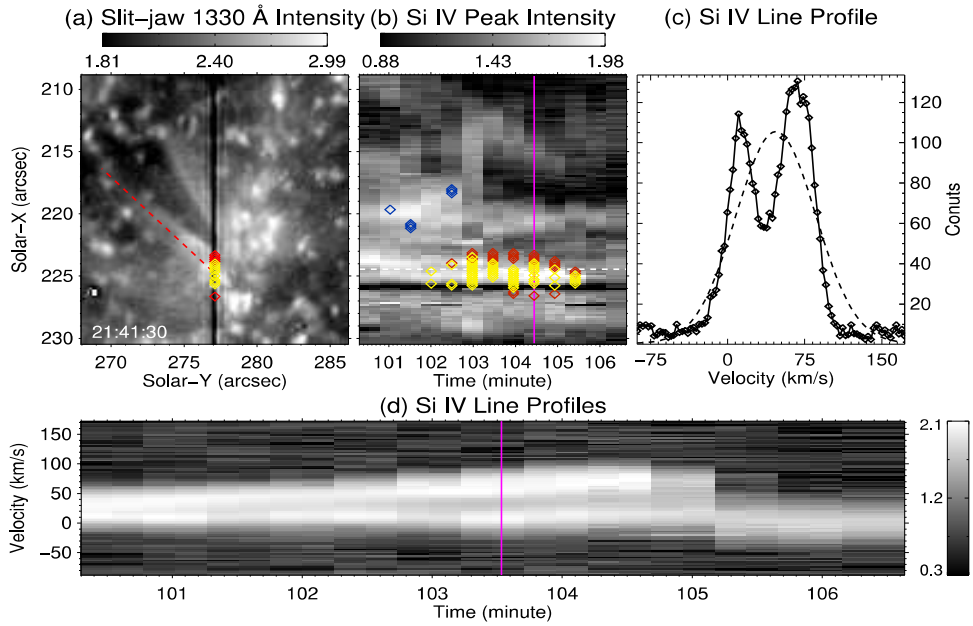

Figure 5.1: The observational data demonstrates (a): SJI 1330 Å image taken at 21:41:30 UT. The red-dashed line in (a) displays the associated spicule-like jet. (b): Temporal evolution of the peak intensity of Si IV 1393.755 Å line profiles. The vertical purple line shows the time of panel (a). The yellow diamonds indicate velocity enhancements in form of two comparable peaks or enhancement in both the wings, while the blue (red) diamonds indicate such enhancement at only the blue (red) wing. (c): Line profile at the intersection of the horizontal dashed line and vertical purple line shown in panel (b). The dashed black line represents the single Gaussian fit. (d): Wavelength (in velocity)−time diagram of the Si IV 1393.755 Å line.

the SJI 1330 temporal image data was 114 s. The details of the observations are given by Chen et al. (2019). Chen et al. (2019) and Huang et al. (2017) have given the criteria for identifying the locations with broadened/velocity enhanced line profiles of Si IV 1393.755 Å , which also infer the clues of impulsive energy release and show the association with the spicule-like jets.

In the present chapter, we revisit a representative observational case reported by Chen et al. (2019) to compare it with our numerical procedure. In addition, we also estimate the length of the observed jet and life-time of the associated velocity enhancement (cf., Fig. 5.1). The same criteria are adopted to identify this localized place in the solar chromosphere

where the unusually broadened line profile is identified in terms of the non-Gaussian profile of Si IV 1393.755 Å line. This location is also found to be associated with the spicule-like jet (cf., Fig. 5.1, 'a'). More details on the IRIS observations and identification criteria of such impulsive locations in the lower solar atmosphere can be found in Chen et al. (2019). It should also be noted that the Si IV 1393.75 Å /1402.77 Å line-ratio can be used to determine whether the ion is formed under optically thick or thin conditions. A ratio close to 2 is particularly compatible with the lines being optically thin (Peter et al., 2014; Yan et al., 2015). We calculated the intensity ratio of the Si IV 1394/1402 Å lines and found that the ratios are always very close to 2. Thus our observations are likely not suffering from the opacity effects. In the present case the double peaked profile of Si IV line is an indicator of the impulsive event going on in the emitting region (Srivastava et al., 2020).

Chen et al. (2019) did not aim to study specifically the properties of the jets associated with the locations where velocity enhancements occurred. In the present chapter, we estimate the length of the spicule-like jet from the SJI 1330 image. The lifetime of the velocity enhancement as estimated using the Si IV line profiles, is also determined in the wavelength (in velocity)-time diagram (Fig. 5.1, panel 'd'). We choose this case as a representative spicule-like jet. The jet is elongated upto the length of 8.0 Mm. We display its spectral/observational analysis in Fig. 5.1. The lifetime of the velocity enhancement is $\sim$ 3.0 minutes for this jet. We conjecture that this episodic behaviour of the Si line profile may be the signature of magnetic reconnection generated impulsive energy release.

Chen et al. (2019) have identified the EEs using the single Gaussian fit because most of the line profiles were single peaked. They used peaks in the residual profile to identify the explosive events. In their study, they further used the double Gaussian fit to the specific profile to derive the Doppler shift at the blue wing. In the present case, we also show a single Gaussian fit in Fig. 5.1 just to illustrate that the profile is indeed deviated from the single Gaussian. Then we fitted the specific double-peak profile again with a double

Gaussian function where we derived the velocity of the second component, i.e., 68 km s^{-1}. Actually, the velocity of the local peak in the residual profile subtracted from the single Gaussian fit is very close to the one derived from the double Gaussian fit, which is about 3 km s^{-1} higher.

As stated above, we subtract the single Gaussian fit from the original line profile, and thereafter find all the peaks in the residual profile. In the next, we consider the peaks with a velocity larger than 30 km s^{-1}, and exclude the peaks around -85 km s^{-1} to avoid Ni II line blend (e.g., Ning et al., 2004). The red-dashed line is drawn to illustrate the spicule-like jet associated with the location where the enhanced velocity in Si IV line profile is obtained (Fig. 5.1, panel 'a'). The observed jets are also visible in the SJI 2796 Å passband but not as clear as the Si IV 1330 Å passband. The observed jet is recorded in transition region Si IV emissions, and they resemble more to the impulsive network jets or hot counterparts of the spicule-like jets. This case is the representative one taken In this chapter to initialize the model spicule-like jet. The observed properties of this jet are used to be compared with the model jet and its evolution.

It is worth mentioning that length of the spicule-like jet may be underestimated due to the projection effects, and the lower cadence of the SJI. It may also be due to the fact that there are many bright points in the SJI 1330 images, and some of them may overlap with spicule-like jets and influence this estimate. The another limitation is that due to the lower cadence of SJI data, we can not resolve the multiple jets (if any) that are associated with the velocity enhancement, therefore, can only determine the approximate lifetime. In the case under consideration here, the lifetime of the velocity enhancement is 3.0 min. The observed event and many likely cases as reported by Chen et al. (2019) may be caused by the strong downflows originated from the reconnection site. It is possible that the slit did not cross the reconnection site, and it only scanned the region with reconnection downflows (Innes et al., 1997a,b). However, the velocity enhancement site is located around the footpoint of the

spicule-like jet, where the reconnection is likely to occur. We put forward that the velocity amplitudes of the downflow and the undetected upflows are roughly equal. In the present chapter the representative case shows a clear two peaks enhancement of Si IV line. The magnetic reconnection may produce bi-directional flows (Innes et al., 1997b), but the slit only crossed part of the reconnection region with downflows. As we interpret these events as a response of underneath reconnection process, we may relate these to the velocity enhancements as seen in Si line profiles most likely due to the impulsive energy release and the formation of upward propagating jets. In conclusion, we observe the location associated with the velocity enhancement in Si IV line profile, most likely due to impulsive energy release, and related spicule-like jet. In the next section, we outline the details of the MHD model regarding formation of the model spicule-like jets. We consider the adiabatic and non-adiabatic conditions of the solar atmosphere in the present numerical simulation.

5.3 Numerical Model of the Spicule-like Jet in Energy Imbalance Condition in the Solar Atmosphere

In order to model a chromospheric cool jet as the response of a velocity perturbation in the solar chromosphere, we consider a gravitationally-stratified and magnetized two dimensional (2-D) solar atmosphere which is governed by a set of MHD equations (e.g., González-Avilés et al., 2021; Mignone et al., 2007a, 2012; Srivastava et al., 2020). The details of the governing equations are given in Chapter 2, Section- 2.4.1.

We consider the adiabatic, and non-adiabatic (cooling effects of radiation and thermal conduction) that exert an impact on the jet evolution and its physical properties. However, we neglect other non-ideal effects such as viscosity and resistivity, and heating of the plasma.

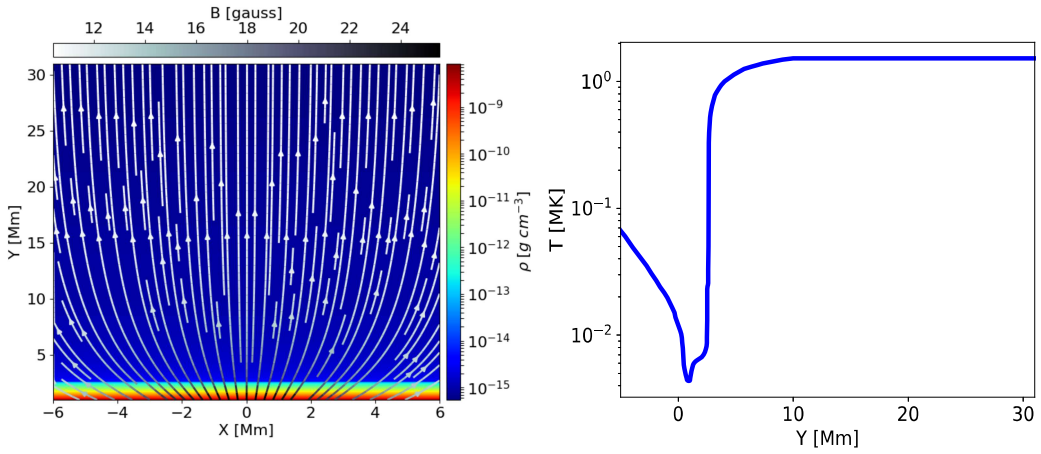

Figure 5.2: Left-panel: Equilibrium unipolar magnetic field vectors in the model solar atmosphere. Right-panel: Temperature profile derived from the model of (Avrett and Loeser, 2008).

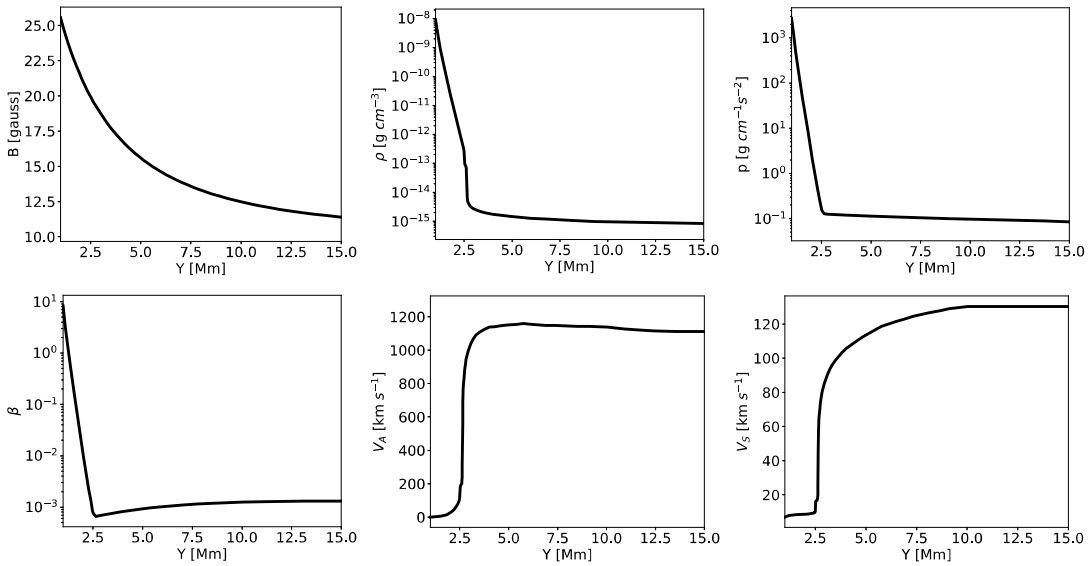

Figure 5.3: The physical properties of the solar atmosphere and their variations with respect to (w.r.t.) height (y) in its equilibrium condition. The top row shows the variation of magnetic field (left), mass density (middle), and gas pressure (right) along the vertical direction of the solar atmosphere. The bottom row illustrates the variation of plasma-beta, Alfvén speed, and sound speed vs. y. The typical values of these characteristic parameters and speeds are well suited for the magnetized solar atmosphere.

The initial magnetohydrostatic condition is implemented into the model solar atmosphere embedded in the PLUTO code. It is described as follows (Srivastava et al., 2020):

$$\mathbf{0} = \frac{1}{\mu}(\nabla \times \mathbf{B}_{\rm e}) \times \mathbf{B}_{\rm e} - \nabla p_{\rm e} + \rho_{\rm e}\mathbf{g}. \tag{5.1}$$

where the subscript "e" depicts equilibrium quantities. We initially consider the current-free magnetic ($\nabla \times \mathbf{B}_{\rm e}$=0) field condition associated with this atmosphere (Low, 1985):

$$\mathbf{B}_{\rm e}(x,y) = \mathbf{B}_{\rm v} + [B_{{\rm e}x}, B_{{\rm e}y}, 0] = [0, B_{\rm v}, 0] + \nabla \times (A_{\rm e}\widehat{z}) \tag{5.2}$$

with the magnetic flux function

$$A_{\rm e}(x,y) = S\frac{x-a}{(x-a)^2 + (y-b)^2}. \tag{5.3}$$

The pole strength S is taken as ≈560 Gauss, and it is located at b=-5 Mm below the bottom of the photosphere at the centre of the simulation box, i.e., a= 0 Mm. The position and strength of the magnetic pole determines the divergence of the magnetic field vectors, which smoothly extend into the overlying atmosphere (Fig. 5.2, left-panel). To mimic a magnetic funnel above a magnetic network we have added a background field of $B_{\rm v}$=10 Gauss.

We use the vertical component of the magnetohydrostatic equilibrium in the described adiabatic model (see Eqs. 2.4-2.9, without adding cooling effects of radiation and thermal conduction terms in Eq. 2.8) solar atmosphere and the ideal gas law to determine the equilibrium gas pressure and mass density w.r.t. the vertical direction (y) as follows (Srivastava et al., 2020):

$$p(y) = p_{ref} exp\left(-\int_{yref}^{y} \frac{dy'}{\Lambda(y')}\right), \qquad \rho(y) = \frac{p(y)}{g\Lambda(y)}, \tag{5.4}$$

where

$$\Lambda(y) = \frac{k_B T(y)}{\hat{m} g}. \tag{5.5}$$

In the above equation, $\Lambda(y)$ is termed as a pressure scale height, $\hat{m}$ is the mean mass, and g=274 m s^{-2} is the magnitude of the gravitational acceleration. In Eq. 5.4, p_{ref} is described as a gas pressure given at the reference level y_{ref}, which lies in the overlying corona at y_{ref}=10 Mm (Srivastava et al., 2020). For the non-adiabatic conditions, the initial state is altered by the thermal conduction and radiative losses. This implements the physical conditions of the energy imbalance in the modeled solar atmosphere, and affects the kinematics and energetics of the simulated jet. The hydrostatic equilibrium is only the initial physical condition when we take into account thermal conduction, radiative loss, or the combined effect of both the mechanism. We aim to understand the effect of energy imbalance conditions on the formation of the cool jets compared to the jets formed in the adiabatic solar atmosphere.

We have tested an energy imbalance in the atmosphere without implementing any velocity perturbation and jet formation (figs. are not shown). In the case of the thermal conduction, there is some energy re-distribution, but still the solar atmosphere remains stable during the period of 180 s of our simulation. Some energy is transported towards the solar chromosphere, which causes the background plasma upflows with nominal speed of less than 10 km s^{-1}. The solar transition region and solar atmosphere remain stable for the entire duration. There is no significant cooling and therefore reduction of the temperature of solar corona. On the similar ground, we have examined the effect of radiative loss and associated cooling. We find that the small background plasma downflows are generated with speed less than 5 km s^{-1}. The entire solar atmosphere still remains stable in terms of its structuring, temperature, and the position of transition region. When we switch on the thermal conduction and radiation both in the solar atmosphere, the thermal conductive losses are re-distributing the energy towards the solar chromosphere, while the radiation

causes the energy loss outward from the solar corona. Initially both plasma upflows and downflows were at work, however, after some time a net small background upflow was present with the speed less than 10 km s^{-1}. The solar transition region as well as entire solar atmosphere is stable for the entire duration. As the time passes, the solar atmosphere tends towards quasi-static equilibrium in all the non-ideal conditions.

5.4 Perturbations

We implement the observed velocity perturbations (V_y=68 km s^{-1}) and perturb the model solar atmosphere in magnetohydrostatic equilibrium by an initial Gaussian pulse in the vertical component of the velocity (V_y). The velocity pulse is defined by the following expression (Srivastava et al., 2020):

$$V_y(x,y,t=0) = A_{\rm v} \times exp\left(-\frac{(x-x_0)^2+(y-y_0)^2}{w^2}\right). \tag{5.6}$$

In Eq. 5.6, (x_0, y_0) represents the initial position of the velocity pulse, and the width of the pulse is given by w. The symbol $A_{\rm v}$ represents the amplitude of the pulse, which is taken as 68 km s^{-1} as deduced by the enhanced line-profile of Si IV 1393.755 Å (see Fig. 5.1). We supply the value of x_0 = 0 Mm, y_0 = 1.6 Mm, and w=0.030 Mm to launch an appropriate velocity perturbations in the chromosphere just below the TR. Such velocity perturbations may be generated due to the conversion of the electromagnetic energy into the outflowing energy of the plasma during the reconnection process in chromosphere. This results into some velocity perturbations at the given chromospheric height. The width of the applied pulse also plays a significant role in the determination of the width of an ejected jet. So, we choose the width as 30 km of the applied pulse such that the width (FWHM) of the jet lies in the observed range of the width of chromospheric spicule-like jets. The choice of the width of the pulse is not related to the IRIS spatial pixel size in the present simulation.

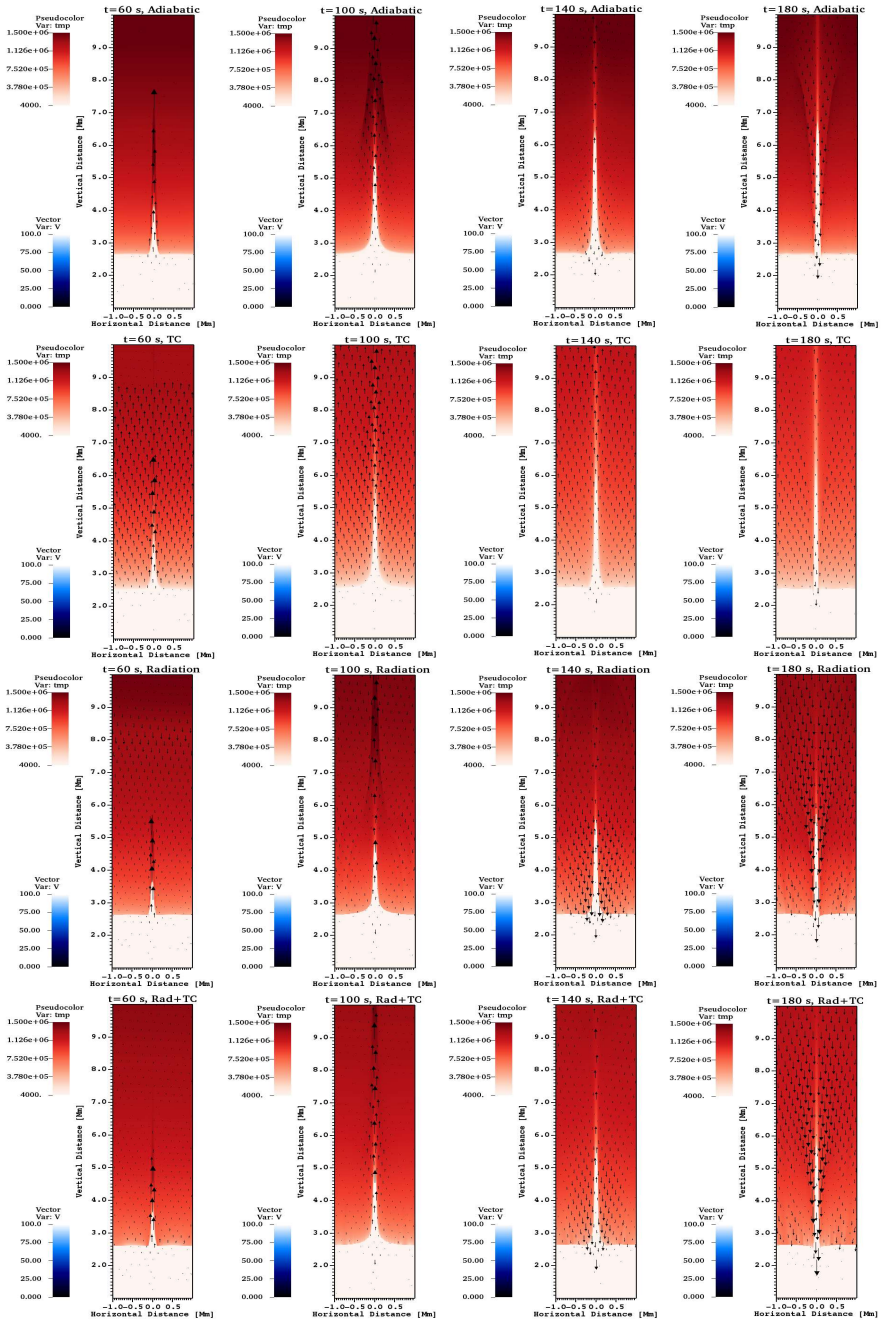

Figure 5.4: Spatio-temporal evolution of the cool spicule-like jet as shown in the temperature maps: First to fourth rows respectively display evolution of the representative model jet in the solar atmospheres under adiabatic condition, thermal conduction, radiative loss, and combined effect of thermal conduction and radiative loss. The velocity vectors are scaled upto the maximum velocity of 100 km s^{-1} as overplotted on different maps.

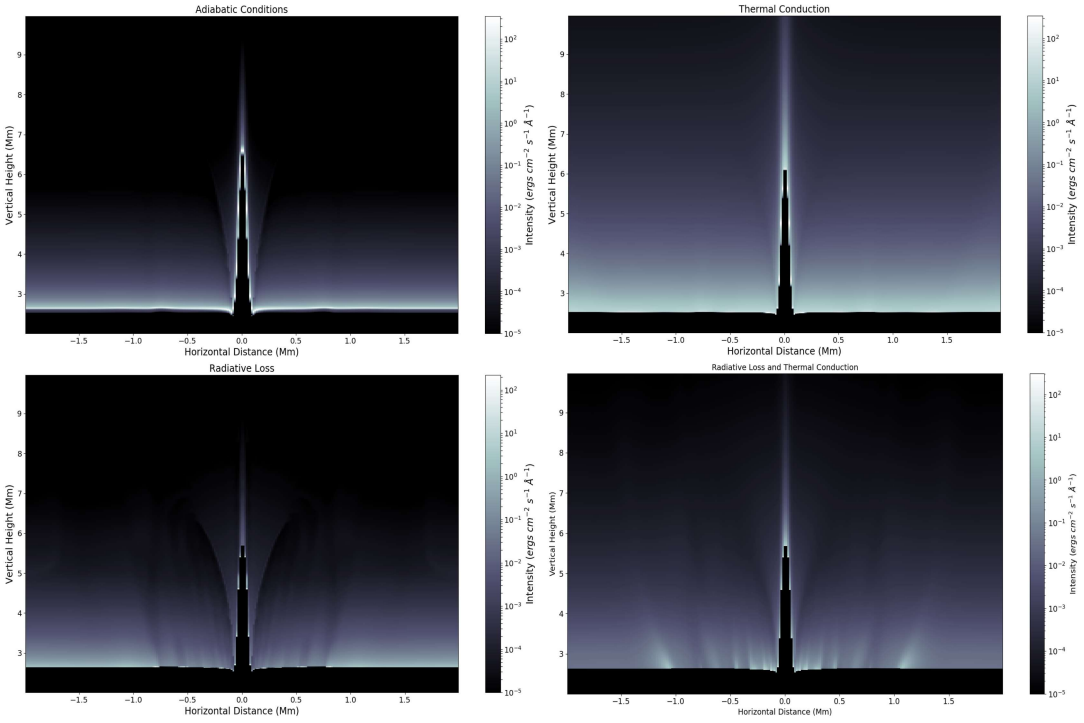

Figure 5.5: Synthetic images in Si IV 1393.755 Å using the simulation data at t=180 s, and CHIANTI Atomic Database: (a) the adiabatic condition (top-left panel); (b) thermal conduction (top-right panel); (c) the radiative loss (bottom-left); (d) joint effect of thermal conduction and radiative loss (bottom-right panel).

Even if the source of perturbations are un-resolved in IRIS, then they result in their action in the form of the observed jets. In the present consideration, we consider its dependence on the grid size. The choice of the width of the pulse should be greater than the size of the grid at the applied location, so that the signal of the pulse could smoothly update through various grids.

The model atmosphere covers the region from the photosphere to the inner corona where open magnetic field lines are present (cf., Fig. 5.2, left-panel). In the model solar atmosphere initially maintained at the magnetohydrostatic equilibrium, the temperature profile T(y) is displayed in Fig. 5.2 (right-panel). This temperature profile is derived from the semi-empirical model of Avrett and Loeser (2008), and its detailed physical description is outlined in Srivastava et al. (2020). The background physical properties of the model

solar atmosphere and their variations w.r.t. height (y) is depicted in various snapshots as shown in Fig. 5.3. The top row of Fig. 5.3 exhibits the variation of the magnitude of magnetic field (left), mass density (middle), and gas pressure (right) in the solar atmosphere. The value of the magnetic field in the solar chromosphere is around 24 G and represents the chromosphere above a strongly magnetized network area in the quiet-Sun where the jets are produced. The bottom row displays the variation of plasma-beta, Alfvén speed, and sound speed w.r.t. y. The typical values of these characteristic physical parameters and speeds are appropriate to the magnetized solar atmosphere, and extend smoothly to its various layers and thus construct a realistic model atmosphere.

5.5 Numerical Methods

The numerical method is embedded in the PLUTO code, which is a Godunov-type, non-linear, finite-volume MHD code (e.g, Mignone et al., 2007a, 2012; Srivastava et al., 2020; Wołoszkiewicz et al., 2014). We constitute a simulation box of the dimension (-6, 6) Mm $\times$ (1, 31) Mm to solve the MHD equations numerically. This simulation box mimics a region of the solar atmosphere 12 Mm wide and 30 Mm high permeated by open and expanding magnetic field lines. All four boundary conditions are fixed to their equilibrium values in order to construct the model solar atmosphere within the simulation box. We have chosen a static uniform grid from x=-6 to x=6 Mm which is divided into 768 identical cells. We have also taken into account a static uniform grids from y=1 to 5 Mm and stretched grids from y=5 to 31 Mm constituting of 256 and 832 cells respectively. The spatial resolution of the model solar atmosphere in the simulation box with a static uniform grid is 15.625 km per numerical cell in both the x- and y-directions, while it is 31.25 km per numerical cell in the y-direction with a static stretched grid. We have stored the simulation data every 10 seconds to capture the dynamical evolution of solar chromospheric jet. In our numerical simulation, we set the Courant-Friedrichs-Lewy number to 0.25. We utilize the

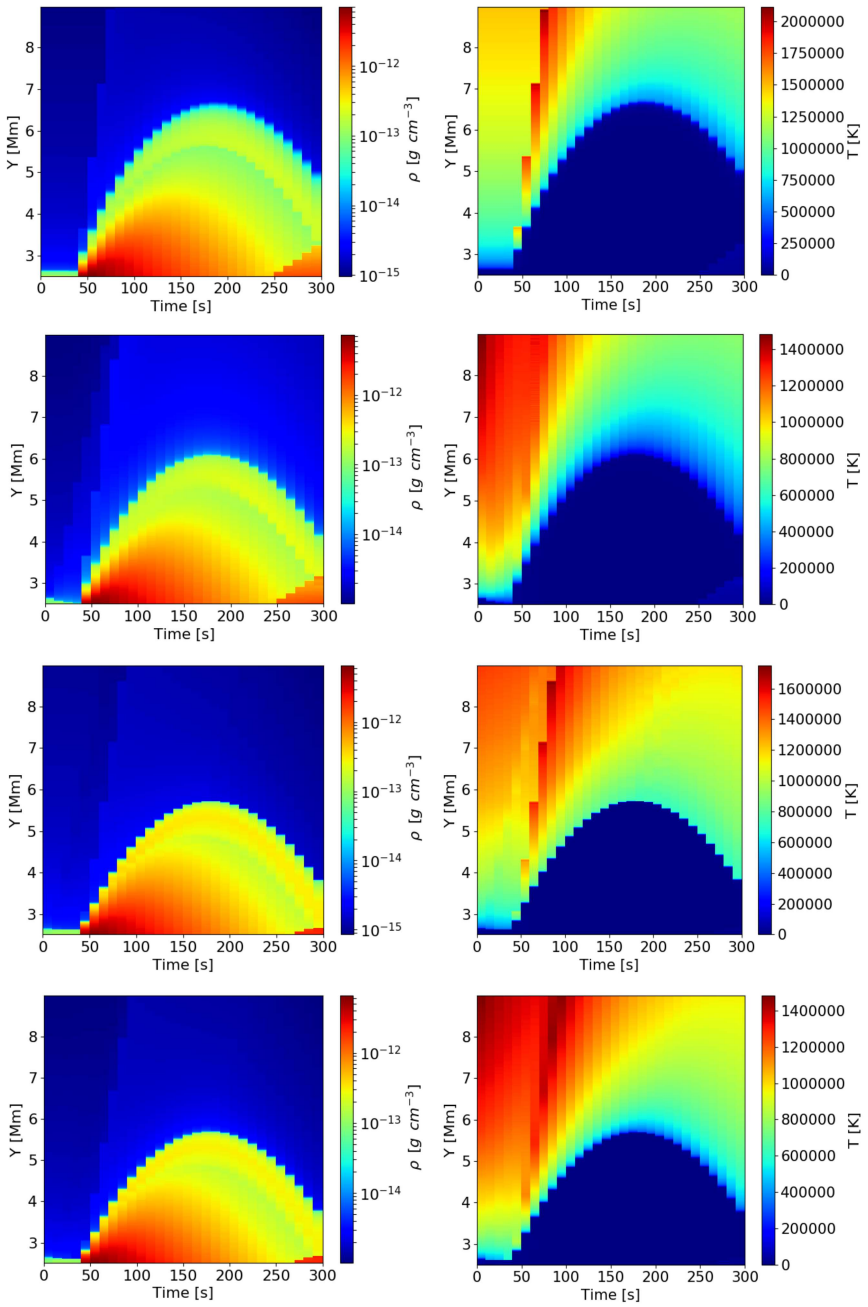

Figure 5.6: Distance time diagrams in density (left-column) and temperature (right-column) of the model jet. The first to fourth rows respectively represent an adiabatic condition, thermal conduction, radiative loss, and combined effect of thermal conduction and radiative loss.

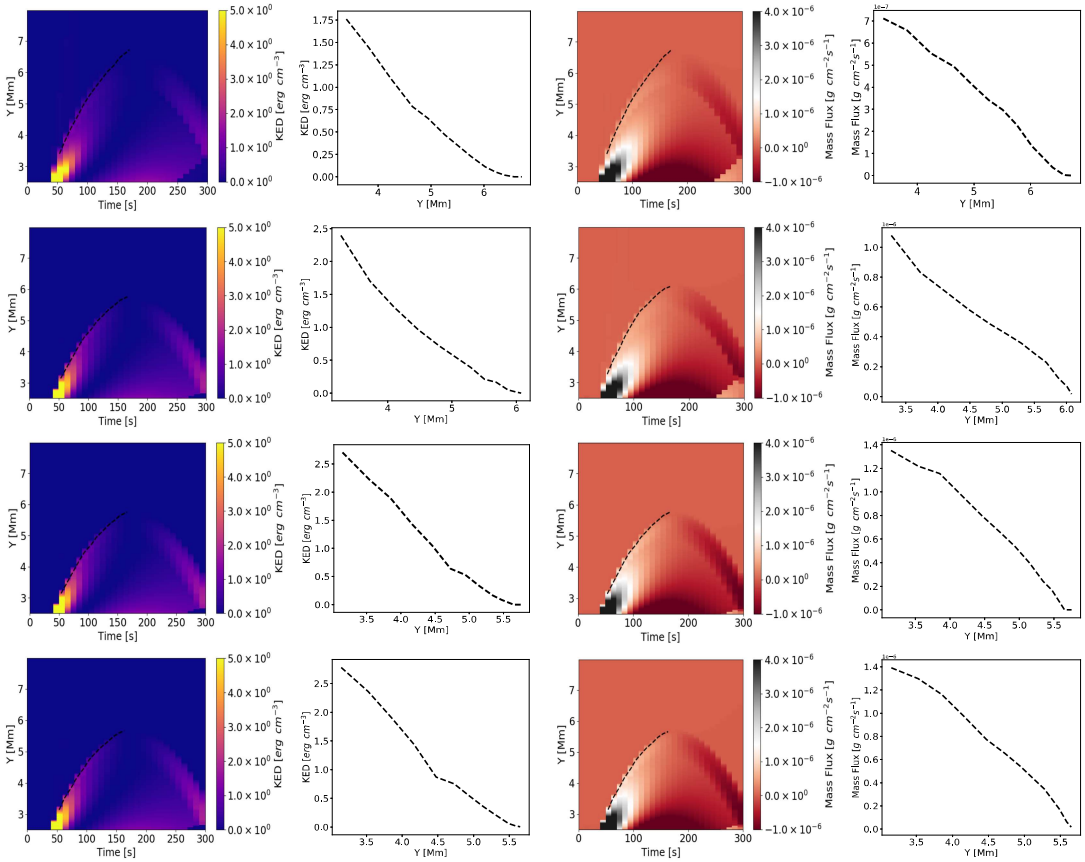

Figure 5.7: The distance time maps of the kinetic energy density (KED) (1^{st} column) and mass flux (MF) (3^{rd} column) are shown during the evolution of jet in the corona. The first row of the panels are related to the estimations in the adiabatic case, second row when only thermal conduction is added, third row when only radiation losses are included, and fourth row when both thermal conduction and radiative losses are considered. The black-dashed paths are overplotted on each of these maps (the 1^{st} and the 3^{rd} column). The KED and MF are estimated w.r.t. the length of the jet along these chosen paths (the 2^{nd} and the 4^{th} column). The spatial distribution of the KED and MF along the jet is basically the manifestation of their values at different temporal epochs when jet is traveling upward.

Roe solver for the flux computation, which is a linearized Riemann solver (cf., Mignone et al., 2007a, 2012; Singh et al., 2019; Wołoszkiewicz et al., 2014). The details of the numerical setup and related methodology can also be found in Srivastava et al. (2020). The details of PLUTO code structure and numerical methods are given in Chapter 2.

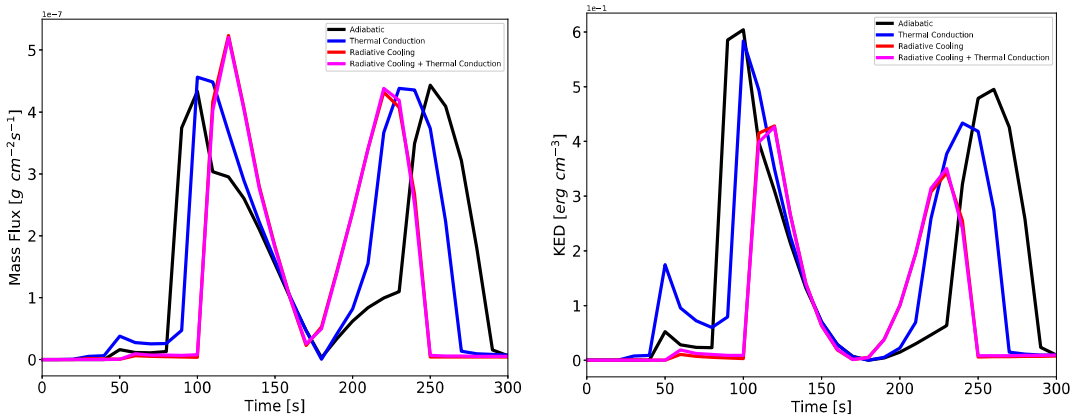

Figure 5.8: Time signatures of mass flux (left-panel) and energy flux (right-panel) estimated at height y=5.0 Mm for adiabatic (black), thermal conduction (blue), radiative loss (red), and combined effect of thermal conduction plus radiation (magenta).

5.6 Evolution of Spicule-like Cool Jets and Their Properties

We construct the representative adiabatic and non-adiabatic models of the spicule-like jet in the solar atmosphere, which consider the implementation of the observed unusual velocity enhancement of 68 km s^{-1} (Fig. 5.1). We perform the numerical simulations by considering the most general scenario that velocity enhancements occurred impulsively and most likely in the lower solar atmosphere. Its observational signature is also recorded in the TR emissions (see Section 2) due to the magnetic coupling of these adjacent atmospheric layers. The Fig. 5.4 displays formation of a cool, thin jet which is produced by the velocity perturbations of 68 km s^{-1} (Eq. 5.6) at the top of the chromosphere. The velocity enhancement perturbs the local hydrostatic equilibrium in the adiabatic model of the solar atmosphere (cf., first-row in Fig. 5.4), and such perturbation grows along the field lines moving towards the much rarefied transition region (TR) and inner corona. The observations (Fig. 5.1) reveal that the velocity enhancements seen in the Si IV line profile, and most likely produced by the reconnection generated impulsive energy release, can

trigger the observed spicule-like jet. The presented results of the numerical simulations exhibit a close matching with these observations. The field aligned velocity perturbations further evolve into the magnetoacoustic shocks, creating a low pressure region behind. This leads to the motion of the collimated plasma forming a jet-like feature along the magnetic field lines (Fig. 5.4, first-row; Fig. 5.5, top-left panel). The cool core material of the jet reaches a maximum height of ≈6.7 Mm in 160-180 s (Fig. 5.4 first-row, top-most panels of Fig. 5.6).

To understand the specific morphological and radiative properties of the simulated jet in connection with the Si IV emissions, we synthesized the EUV emission intensity I_λ (ergs cm^{-2} s^{-1} Å $^{-1}$) of the observed spectral line Si IV 1393.755 Å (Del Zanna and Mason, 2018).

$$I = \int_s G(N_\mathrm{e}, T)\, N_\mathrm{e}\, N_H \, \mathrm{d}s \tag{5.7}$$

The contribution function G is given by:

$$G(N_\mathrm{e}, T) = Ab(Z)\, A_{ji}\, \frac{1}{4\pi} \frac{hc}{\lambda} \frac{n_j(T, N_e)}{N_e} F(T) \qquad [erg\ cm^3\ sr^{-1}\ s^{-1}] \tag{5.8}$$

For generating the synthetic images in Fig. 5.5, we have used ChiantiPy database [1]. We have computed the emission intensity of Si IV 1393.755 Å line at every grid point in the numerical simulation domain at t = 180 sec. We use the intensity calculator function in ChiantyPy. Intensity in ChiantiPy is calculated as a function of temperature and density. ChiantiPy first estimates the contribution function $G(T, N_e)$ given by Eq. 5.8 where T is the plasma temperature, N_e is the electron number density, h is the Planck constant, c the speed of light, n_j is the population of the upper emitting level of the transition relative to the total population of the ion, $F(T)$ is the ionization fraction of the emitting

[1] https://www.chiantidatabase.org/tech_reports/03_synthetic_spectra/chianti_report_03.pdf

ion, and A_{ji} is the radiative decay rate for the transition. Ab(Z)= N_{Si}/N_H is the abundance function. The temperature and density is taken from the numerical simulation data, while the atomic parameters for Si IV 1393 Å transition are taken into account from Chianti Atomic Database (Dere et al., 1991, 2009). The intensity at each and every point in the numerical domain is calculated using the Eq. 5.7 where $G(T,N_e)$ is the contribution function calculated in the previous step. We have performed this synthesis to verify our numerical simulations with the synthetic spectral emission data which is closely related to IRIS Si IV 1393 Å at the numerically simulated temperatures and density. As far as this 2-D synthesis is concerned, it is encompassing an optically thin radiation of the Si IV ions. The CHIANTI based synthetic images are generated using Eqs. 5.7, 5.8 and by excluding the complexities of observed line-profiles of Si IV 1393.755 Å , and its objective is to just show that the observed jets can be synthesized in Si IV Transition Region (TR) emissions using basic simulation parameter (e.g., density, and temperature) and CHIANTI atomic parameters. We leave the integration process along the independent axis of the 2D simulation which is perpendicular to the panels of Fig. 5.5. In exercising such a procedure, we assume the existence of an isothermal plasma along the line-of-sight at each and every height in the model solar atmosphere. This simplified assumption although works well in the present 2-D simulations where solar atmosphere is structured in y-direction (Fang et al., 2015), while at each height it is treated isothermal in the ignorable another horizontal coordinate (i.e., z-coordinate).

We compute intensity assuming optically thin plasma over each grid as defined by the spatial resolution of the numerical simulation data. We choose the same spectral line for the synthesis, which is utilized earlier to deduce the spectral properties (Fig. 5.1) in form of velocity enhancement/line-profile broadening, and its life-time. It provides a close and reasonable match with the SJI Si IV 1330 Å image in which the associated jet is detected and shown in the panel 'a' of Fig. 5.1. The synthetic images at t=180 s, when jet reaches

to the maximum height in the solar corona, are presented in Fig. 5.5 for adiabatic (top-left), thermal conduction (top-right), radiative loss (bottom-left), and joint effect of thermal conduction and radiative loss (bottom-right) cases respectively. As far as adiabatic case of the numerical simulation is concerned (Fig. 5.4, first-row), it is clear that synthetic image displays some interesting physical scenario. The Si IV emission, which is a predominant TR/inner coronal emission, envelopes and constitute the outer layer of the jet. This is a hot TR plasma that is seen in form of the well evolved jet, and resembles with the observations (Fig. 5.1,'a' and Fig. 5.5, top-left panel). The TR counterpart of the model jet is reached to the observed height of the spicule-like jet, i.e., 8.0 Mm (Fig. 5.1, 'a'). However, we also see a typically cool counterpart of the jet material, which lies within TR counterpart and represents a core cool material reaching upto the height of ≈6.7 Mm. This cool component of the jet will not be evident in the comparatively high-temperature emissions of Si IV as seen in the observations in Fig. 5.1. However, in the synthetic images of the simulation map, it is clearly seen that the jet's observational manifestation is its outer-layer made-up of comparative hot plasma emitting in Si IV TR lines. While, its core is made-up of cool chromospheric material ($\approx 10^4$ K), which is seen as a dark structure in this TR emissions. Such a typical scenario of the spicule-like jets are commonly observed recently when the chromospheric material of the jet is heated quickly upto the TR and inner coronal temperatures (1 MK), thereby seen in the corresponding emissions (e.g., De Pontieu et al., 2011; Kayshap et al., 2018; Pereira et al., 2014; Rouppe van der Voort et al., 2015, and references cited therein). We basically demonstrate that how the simulated jet will be seen if we synthesize it in IRIS SJI Si IV 1393 optically thin emissions. We do observe the on-disk jet as seen in IRIS SJI (Fig. 5.1). However, in the numerical simulation the solar atmosphere is structured in the y-direction. In the numerical simulation domain, the solar atmosphere is shown structured in the y-direction, i.e., all the background physical parameters such as density, pressure, temperature, sound speed, Alfvén speed are varying

with only vertical (y) direction (see Fig. 5.1-5.3), however, certainly not along horizontal direction. These physical parameters smoothly extended from the photosphere (0.0 Mm) up to inner corona (30 Mm) via chromosphere and transition region in the considered model of gravitationally stratified solar atmosphere. So there is nothing like on-disk or limb representation of the numerical simulation in the present simulations. The observed jet which is visible on the solar disk is modelled in 2-D, ideal and non-ideal atmosphere moving up into the higher atmosphere. The model jet is triggered upward in the inner corona due to velocity enhancements in the solar chromosphere. The synthetic images demonstrate that Si IV emissions are from the TR plasma which is making the outer envelope of the cool model jet as seen in the SJI observations. In the Fig. 5.5, bottom-left panel, we see some downfalling cooled plasma due to radiative loss, and they are seen as black features in the Si emissions. In the bottom-right panel, some bright transition region plasma visible in Si IV emissions are seen as background outflowing plasma around the jet. In the simulation under the effect of radiative loss, we detect the plasma downflows around 5 km s^{-1} even there was no velocity pertubations implemented. Doschek et al. (1976) have analysed the solar transition region lines and found that the transition region plasma is downflowing (red-shifted plasma) with an average speed of 15 km s^{-1}. The difference between TR downflows and realistic red-shifted velocity of TR may be due to the fact that a certain cut-off temperature is utilized while implementing the radiative loss model in the optically thin plasma, which is 10,000 K and rather idealistic consideration given the complexities of solar atmosphere.

The distance time diagrams for the density (left-column) and temperature (right-column) of the model jet are displayed in Fig. 5.6. The first to fourth rows of this figure respectively display the distance-time diagram of the model jet in the adiabatic condition, thermal conduction, radiative loss, and under the combined effect of thermal conduction and radiative loss. All the distance time diagrams are made by choosing the

vertical slit between y=2.5-9.0 Mm at x=0.0 Mm, which passes through the jet at its central axis. The cool core material of the model jet reaches to the height of 6.7 Mm (cf., first-row in Fig. 5.4 & 5.6) in the adiabatic case once it is launched by the velocity pulse of 68 km s^{-1}. However, it can be clearly seen that the TR counterpart of the jet's plasma is seen even upto the height of ≈9.0 Mm (cf., Fig. 5.4, first-row; see synthetic image in Fig. 5.5, top-left panel). The magnetoacoustic shock front is also clearly visible developing in the adiabatic atmosphere due to the growth of the velocity perturbations in the chromosphere. The field aligned velocity perturbations propagate into the stratified solar atmosphere and steepen in form of the magnetoacoustic shock (cf., t=60-100 s panels in the first-row of Fig. 5.4). However, the shock leaves the simulation domain/model atmosphere quickly. The shock creates an under pressure region below it, which launches cool plasma jet. The shock propagation is also clearly visible in the distance-time diagram in the first-row of Fig. 5.6. The height of the TR counterpart of model jet (Fig. 5.5, top-left panel) is close to the observed height of 8.0 Mm as seen in the IRIS SJI image (cf., Fig. 5.1, 'a').

Note that under the effect of thermal conduction, the energy of the jet and background plasma both are re-distributed in the solar atmosphere. Subsequently the less energized cool core material of the jet reaches to the height of 6.0 Mm only (cf., second-row in Fig. 5.4; (e.g., Antolin, 2020; González-Avilés et al., 2021)). The re-distribution of the energy due to the thermal conduction causes bulk upward flows in the ambient solar atmosphere as seen in the second-row of Fig. 5.4. This episodic energy imbalance affects the morphology, height, and kinematics of the jet (González-Avilés et al., 2020). However, the upward background flows tries to enhance the kinetic motions (or higher velocity) of the TR counterpart of the jet. It is still visible at the higher altitudes moving at ≈9.0-10 Mm as some plasma flows are also evident there (cf., t=180 s panel in Fig. 5.4, second-row; synthetic image of Si IV in Fig. 5.5, top-right panel). The denser core of the jet is cooled by the thermal conductive losses (cf., left-panel in the second row of the distance-time

diagram in Fig. 5.6). However, its outer transition region counterpart moves to higher heights due to upward plasma flows in the background corona. The much longer jet is visible in the Si IV emissions (see the synthetic image in the top-right panel of Fig. 5.5). Another important aspect is that the upward propagating magnetoacoustic shock above the moving jet is dissipated due to the effect of thermal conductivity (second row of Figs. 5.4 & 5.6). The solar atmosphere is in energy imbalance condition for a certain duration due to the thermal conductivity, and the temperature of the corona is slightly decreased, but it is still maintained at around 1.0 MK. The solar transition region also remains stable.

The radiative loss also significantly affects the formation of the jet (cf., third row in Figs. 5.4 & 5.6; bottom-left panel in Fig. 5.5). The background environment is not in energy balance, and radiative cooling of the coronal plasma affects the jet formation. It can be seen in the third row of Figs. 5.4 & 5.6 when the jet's core plasma reaches only upto the height of 5.6 Mm in the presence of the radiative cooling. However, the TR counterpart of the jet reaches upto 7.5 Mm (bottom-left panel in Fig. 5.5), which is close to the observed jet of the length 8.0 Mm as seen in the Si IV TR emissions captured by IRIS (Fig. 5.1, 'a'). There is no heating term introduced here because this allows us to examine how this jet is affected by the radiative cooling. The shock front appears ahead of the jet, however, it is dissipated a little only. The shock front is not evolved well likewise it was seen in the adiabatic case (cf., Fig. 5.4, the first & third rows). For the given duration the solar transition region remains stable and coronal temperature is also maintained around 1.0 MK.

The combined effect of the radiative cooling and thermal conduction on the jet is shown in the fourth-row of Fig 5.4 and in the synthetic image (bottom-right panel of Fig. 5.5). It is clear that the radiative cooling dominates over the thermal conductive effects as the cool core plasma of the model jet attains almost similar height (≈5.6 Mm; fourth-row in Fig. 5.6) as seen in the radiative cooling case alone. However, the TR counterpart of the jet

reaches upto ≈7.5 Mm, which is close to the observed value (cf., bottom-right panel of Fig. 5.5). When the thermal conduction re-distributes the energy, and generate resultant upflows, on the same time optically thin radiative loss is cooling the coronal plasma and resulting the downflows. The radiative loss and associated plasma downflows dominate in the beginning and affect the jet motion. The shock front appears ahead of the jet, however, it is also dissipated quickly. The shock front is not evolved well compared to the one seen in the adiabatic case (cf., Fig. 5.4, first and fourth-row). Inspite of the energy imbalance and subsequent counteracting plasma flows, the temperature of the corona is maintained around 1 MK and transition region remains stable in the given duration of time.

In the first column of Fig. 5.7, the distance time map of the kinetic energy density (KED in ergs cm^{-3}) is presented during the evolution of the jet. The cases of adiabatic (the 1^{st} panel in the first -row), thermal conduction (the 1^{st} panel in the second-row), radiative loss (the 1^{st} panel in the third-row), and the combined effect of radiative loss and thermal conduction (the 1^{st} panel in the fourth-row) are shown in the subsequent images. The black-dashed path is overplotted on each of these maps. Along these path the KEDs are estimated w.r.t. the length of the jet in each case. The estimated KEDs w.r.t. the distance are respectively shown for the adiabatic (the 2^{nd} panel in the first-row), thermal conduction (the 2^{nd} panel in the second-row), radiative loss (the 2^{nd} panel in the third-row), and under the combined effect of radiative loss and thermal conduction (the 2^{nd} panel in the fourth-row). In the third column of Fig. 5.7 (from top to bottom panels), the distance time maps of the mass flux (MF in gram cm^{-2} s^{-1}) are shown in the adiabatic, thermal conduction, radiative loss and combine effect of the radiative loss and thermal conduction respectively during the evolution of the jets in the corona. The black-dashed path is overplotted on each of these maps over which the MF is estimated w.r.t. the length of the jet displayed in the 4^{th} column respectively.

MF is estimated using mass density and signed vertical velocity within the jet. It should be noted that the spatial distribution of the KED and MF along the jet is basically their values at different instances when the jet is traveling upward. We assign a positive and negative sign respectively to the upward and downward moving mass flux. The corresponding distance time maps with appropriate colour bar scheme are displayed in the third column of Fig. 5.7. We take into account this scheme to show the upward and downward motion of the jet plasma. The opposite colour contrast on the evolved parabolic paths in the distance time map of the mass flux (the 3^{rd} panels in first to fourth rows in Fig. 5.7) display upward and downward moving plasma associated with the jet motion. We trace a path (black dashed curve) on the rising part of parabola as shown in the mass flux distance time diagrams. We estimate the variation of the mass flux w.r.t. height along the jet (Fig. 5.7, third and fourth columns). It should be noted that when the jet reaches a maximum height, it contributes the mass flux of the order of 10^{-7} g cm^{-2} s^{-1} for the adiabatic case (cf., the 4^{th} panel in the first-row in Fig. 5.7) at different heights in the solar atmosphere. The core cool material of the jet associated with the non-adiabatic conditions, e.g., thermal conduction (cf., the 4^{th} panel in the second row), radiation (cf., the 4^{th} panel in the third row), and combined effect of thermal conduction and radiative loss (cf., the 4^{th} panel in the fourth row) reach at the shorter heights, however, they are much denser and carry larger amount of the mass flux compared to the adiabatic case. As soon as these jets reach to their maximum height, they do not transport mass flux upward. It looks obvious behaviour of the jet but this is not the complete physical scenario until we do not analyze the details of Fig. 5.8 (left-panel). In this figure, the mass flux imbalance is evident at certain height in the inner corona between the upward and downward moving plasma associated with the jet. However, before going to analyze it in detail, we first infer that the first and second column of Fig. 5.7 show the distance time maps of KEDs of the model jets in adiabatic and non-adiabatic conditions. The KED at each and every height is calculated

by $\frac{\rho v^2}{2}$. Under the adiabatic condition, the jet consists of reasonable KED at different spatial locations between ≈3.4-6.4 Mm as ≈1.76-0.02 ergs cm^{-3} or ≈0.176-0.002 J m^{-3} . This matches well with the recent estimation of the KED in macrospicules (González-Avilés et al., 2021). The jets associated with the non-adiabatic conditions, e.g., thermal conduction, radiative loss, and combined effect of thermal conduction and radiation reach at the shorter heights, however, they are much denser jets and carry larger amount of KEDs compared to the adiabatic case. It should be noted from the panels in the second column of Fig. 5.7 that when the jet reaches to its maximum height, at different spatial locations in different temporal spans, it carries the kinetic energy density.

The left panel of Fig. 5.8 shows the variation of mass flux with time along a horizontal strip taken at y=5 Mm on the distance time maps in both the adiabatic and non-adiabatic cases. These variations exhibit a temporal evolution of the mass flux associated with the jet once it crosses 5 Mm height (first peak in left-panel of Fig. 5.8), and thereafter falls back through the same point (second peak in left-panel of Fig. 5.8). This clearly depicts that the rise and fall of the plasma has a difference in the mass flux at the detection point at y=5 Mm in case when radiative loss is dominant (see the magenta and red curves in left-panel). It is interesting to note that the adiabatic case (black-curve) does not cause any mass flux imbalance, however, the thermal conduction (blue-curve) causes a little imbalance in the mass flux. This infers that the radiative loss (along with thermal conduction or alone) produces shorter (cf., Figs. 5.4-5.6) and bulky jets (Fig. 5.7). The radiation dominating atmosphere yields some small fraction of the plasma moving higher into the corona, and not all the mass falls back. In this case, the mass flux returning back to the detection point is 20% less compared to the mass flux went upward during the jet motion. This difference of the mass flux is ≈1.2×10^{-7} g cm^{-2} s^{-1}. The right panel of Fig. 5.8 shows the variation of KEDs with the time along a horizontal strip taken at y=5 Mm on the time-distance map (cf., first and third columns of Fig. 5.7). This variation exhibits a temporal evolution of the

KEDs associated with the jet once it crosses a height of 5 Mm (first peak in right-panel of Fig. 5.8), and thereafter falls back through the same height (second peak in right-panel of Fig. 5.8). This imbalance of the rising and falling jet plasma also possesses a difference in the KED at the detection point at y=5 Mm. This difference of the kinetic energy per unit volume is largest ≈0.15 ergs cm^{-3} or ≈0.015 Joule m^{-3} (cf., blue-curve in right panel of Fig. 5.8) in the case of thermal conduction. This is the manifestation of the re-distribution of energy due to thermal conduction. It results background upflows launching more energetic chromospheric jets (cf., Figs. 5.4, 5.5). This scenario also indicates that while the jet returns back to this detection point, it has already lost ≈25% of its kinetic energy. The jet in adiabatic case (cf., black-curve in right panel of Fig. 5.8) also shows the energy imbalance, however, lesser than the same in the case of thermal conduction. The radiation (red-curve) and combined effect of radiation and thermal conduction (magenta-curve) also exhibit the energy imbalance, however the extent is small in these two cases. The energy imbalance observed here is not an indication of the dissipation, however, it is related with the fact that some fraction of the mass carries out the momentum ahead in the higher corona, and it is essentially related with the fraction of mass transport in the overlying corona (Fig. 5.7).

In conclusion, the difference of the mass flux during upward and downward motion of a particular jet up to the inner coronal heights infers that most of the mass launched by the jet is returned back to the lower part of the solar atmosphere, however, some amount of the mass flux can still follow to the outgoing shock and can be launched into the corona. This less denser and faint mass motion is not visible though but may contribute to the mass transport in the background coronal plasma. There may be a possibility that it can also contribute to the nascent solar wind. The most of the kinetic energy within the jet also changes between kinetic and potential energies (left-most column of Fig. 5.7). However, a little energy imbalance between upward propelled and downward falling jet plasma may

be due to the fact that some momentum is carried away by the lost tiny mass fluxes from its cool core material reaching upward in the overlying corona. In comparison to the height (≈8.0 Mm) of the presented jets moving with a subsonic speed, the height of the simulation box (i.e., model corona) is sufficiently large (30 Mm). Therefore, the estimation of MFs and KEDs imbalance as well as their lost fractions are not affected by any boundary effects. The physical effects of adiabatic and non-adiabatic conditions are explained in detail above. The radiative loss helps in triggering less energetic, shorter, but bulky jets where some fraction of the plasma can also be launched at the coronal heights. However, the thermal conduction results in the comparatively longer, energetic, but less bulky jets. Such jets are not be able to launch some significant mass fraction to the overlying corona, however, they can provide some larger momentum to the upward moving mass flux within the jet. The model jets have the TR counterparts visible in the synthetic Si IV 1393.75 Å emissions (Fig. 5.5) identical to the observed jet in IRIS (Fig. 5.1). However, they possess the typical cool counterparts as a core jet material that can be identified in the pure low chromospheric emissions only in the observational base-line (Pereira et al., 2014).

5.7 Discussion and Conclusions

A variety of the jets can have a common site of origin to that of chromospheric spicules, i.e., chromospheric network boundaries where magnetic field concentration is large and intermittent reconnection can occur (Yang et al., 2018b). The localized energy release due to the small-scale magnetic reconnection at the boundaries of the magnetic network is proposed to be a triggering mechanism for the formation of network jets, and even episodically the solar spicule-like jets (e.g., type-II; macrospicules, network jets, etc) (Kayshap et al., 2018; Samanta et al., 2019; Sterling, 2000; Wilhelm, 2000). There is a recent report that typical chromospheric spicules can also be generated by the magnetic reconnection (Samanta et al., 2019). Recent IRIS observations have shown that localized impulsive energy release

may broaden the profiles of Si IV lines (e.g., Chen et al., 2019; Huang et al., 2014, 2015; Rao et al., 2019, and references cited there). The velocity enhancements are evident in the spectral lines of different chromospheric regions, e.g., plage regions where cool magnetic loops are anchored (Huang et al., 2015; Rao et al., 2019), the flux tubes at the network boundary where chromospheric jets originate (Chen et al., 2019), etc. Recently, Srivastava et al. (2020) have implemented velocity enhancement features as observed by IRIS in a model atmosphere where a low-lying bi-polar magnetic field system was perturbed in the chromosphere below the TR by a velocity pulse with a maximum amplitude of 200 km s^{-1}. The data-driven 2-D numerical simulation showed that the plasma motions evolved in a similar manner as observed by IRIS in the context of the formation of cool loops (Huang et al., 2015; Rao et al., 2019). The flowing cool plasma fills a cool loop system, which was very dynamic in nature. Srivastava et al. (2020) have reported that the evolution of a flowing cool loop is associated with the velocity response of the transient energy release above their footpoints in the chromosphere/TR. The observations vis-á-vis modeling have provided the information that the velocity perturbations, most likely associated to the EEs as their indirect effect on the chromospheric/TR plasma, could be one of the primary physical processes for the evolution, dynamics and energetics of the flowing cool loop system (Huang et al., 2015; Rao et al., 2019; Srivastava et al., 2020).

In the present chapter, a representative example of the unusual line broadening of Si IV 1393.755 Å line have been observed in a chromospheric magnetic network region, and the corresponding velocity enhancements are recorded along with its life-time and formation of associated jet (Fig. 5.1). The observed velocity enhancement/perturbation is most likely associated with the indirect response of the localized impulsive energy release, and it is estimated as 68 km s^{-1}. The lifetime of the velocity enhancement is found to be ≈3.0 min. The jet is found to be associated with this velocity enhancement, and possess a length of 8.0 Mm. We revisited the data set used by Chen et al. (2019) to analyse a specific jet event, and

specifically performed in the present chapter to initialize the numerical model accordingly, and to compare and match the properties of model and observed jets. Such events may be highly energetic, localized phenomena which may be present ubiquitously in the quiet and active Sun. In the present case, the numerical simulations have been done by considering the most general physical scenario that velocity enhancements occurred impulsively and most likely in the solar chromosphere whose observational signatures are also observed in the TR Si IV emissions as described in Section 5.2. Such velocity perturbations produce both hot TR and cool chromospheric components of the spicule-like jets (cf., Fig. 5.5) (Pereira et al., 2014). The modeled jets are impulsively originated, and they are obviously not associated with any traditional/gentle flow structures or the perturbations of the solar phtosphere and/or the solar chromosphere. In the present chapter, we conjecture that the magnetic reconnection may cause the velocity enhancement/perturbation in the solar chromosphere, which is visible from non-Gaussian line profile (Fig. 5.1). Later on, the velocity perturbations trigger the spicule-like jets because in the lower part of the solar atmosphere they will not have a direct physical response in terms of Lorentz force. Instead, the velocity perturbations will generate shocks, and plasma will follow behind it in the low pressure region in the solar chromosphere. Such a magnetohydrodynamics/hydrodynamic response of the lower solar atmosphere is well studied in the formation and evolution of the plasma in a variety of magnetic structures, and depend upon the localized physical and magnetic field conditions there (e.g., Kayshap et al., 2013b; Shibata et al., 1982; Singh et al., 2019; Srivastava et al., 2020, and references cited there). The observed jets are not the direct magnetic force driven outflows themselves, but they are the plasma outflows linked with the response of the unusual velocity enhancements associated with reconnection generated impulsive energy release in the solar chromosphere. In the recent observations, Panesar et al. (2020), have found that the small-scale jets, network jets, at the base of small filaments/loops occurred due to magnetic reconnection process, which

further drive the plasma outflows. In the present chapter we do not directly observe or model the reconnection events, however, we can speculate similar scenario here for the solar atmosphere that reconnection generated energy release and subsequent velocity perturbations at small-scale originate the cool jets. In the present case, the reconnection generated localized energy release and velocity perturbations in the chromosphere may generate magnetoacoustic shocks in the overlying TR/corona and cool plasma follows in form of the spicule-like jets.

The observational event was associated with the formation of the cool chromospheric jet near the coronal hole. We implement the observed velocity enhancement in a gravitationally-stratified, magnetized 2-D model solar atmosphere, which consists of open and expanding magnetic fields resembling coronal hole and realistic temperature profile, to yield thin plasma jet whose properties closely resemble with the observed jet. The representative case of a jet driven by a velocity pulse of 68 km s^{-1} has been demonstrated. The most of the kinetic energy density (KED) and mass flux (MF) remained confined to the jet, while some small fraction of the mass (max 20%) is lost to the upward region in the model solar coronal hole in case when we consider the energy imbalance due to the radiative losses. This lost mass flux is very small, i.e., 10^{-7} g cm^{-2} s^{-1} when we compare with the bulky jet, and most of the jet's plasma falls back onto the solar surface. However, when we note the chromospheric mass loss to the nascent solar wind above coronal holes, it is only 2×10^{-10} g cm^{-2} s^{-1} (Withbroe and Noyes, 1977). Therefore, the mass flux transported by a velocity pulse driven chromospheric network jet into the overlying corona permeated by the open field lines (10^{-8} g cm^{-2} s^{-1}) is sufficient to compensate the mass loss by the solar wind. However, the major question is the filling factor of such jets into the solar corona and their occurrence frequency. Moreover, it is most likely scenario that the lost energy (or momentum) of the jet is utilized in launching this small fraction of the mass in the overlying model solar atmosphere. The spectroscopic observations show that some cool

jets often reveal blueshifts and seldom redshifts (Tian et al., 2014), however, our model invokes the downfall of the plasma and only a small mass loss. This difference may be due to the fact that those observed jets become faint mostly after their launch against the highly dynamic, bright, and magnetically complex chromospheric/TR background atmosphere so the downfall is not observed there.

In conclusion, the present model demonstrates the formation of the spicule-like jet due to an episodic velocity enhancement, which may be most likely associated with the response of the impulsive energy release in the upper chromosphere/TR as observed in the IRIS observations. The velocity enhancement/perturbation provides significant amount of kinetic energy (Fig. 5.7) and momentum to the plasma, thus resulting in the formation of the jet. We do not discard other mechanisms that might yield the chromospheric spicule-like jets, e.g., magnetic reconnection driven by a combination of magnetic flux emergence and horizontal advection (Yang et al., 2018b), release of twist during magnetic reconnection and formation of rotating jets (Kayshap et al., 2018; Pariat et al., 2015), etc. However, the main scenario for the formation of our observed jet supports the localized small-scale reconnection and energy release in the upper chromosphere/TR (e.g., Kayshap et al., 2018; Panesar et al., 2018, 2019; Tian et al., 2014, references therein). The present study is unique in the sense that it invokes a spectral signature of the velocity enhancements in the TR and the formation of associated jet. There may be any specific physical scenario at the work in the solar chromosphere as mentioned above (e.g., small-scale flux emergence and cancellation; reconnection between twisted and open fields, etc), however, the ultimate response of it is recorded by IRIS in the form of unusual velocity enhancement in Si IV line profile that subsequently trigger the cool spicule-like jet. Our model does not argue on the possible origin of the velocity perturbation. It only focuses on the triggering of the spicule-like jet due to the observed velocity enhancement in the lower solar atmosphere, and its propagation in the overlying corona under the adiabatic and non-adiabatic physical

conditions. It is well noted in the present chapter that the energy imbalance (thermal conductive and/or radiative losses) affects the jet propagation, kinematics, energetics, and its mass and energy contributions to the inner corona. The model jet has its TR counterpart visible in the synthetic Si IV 1393.75 Å emissions (Fig. 5.5) identical to the observed jet in IRIS (Fig. 5.1). The jet's plasma is visible in TR emissions in both the adiabatic and non-adiabatic cases. However, such jets also possess the typical cool counterparts as a core material that can be observed only in the typical chromospheric emissions (Pereira et al., 2014). More detailed observational studies, and stringent numerical modeling are required to understand in greater detail the driving mechanisms of such jets in general and their direct connection with the observational signature, physical properties, and their role in the highly dynamic solar atmosphere. Therefore, our model provides scientific results In this chapter with some new information that the origin of the spicule-like jet can be linked to the response (e.g., velocity perturbations) of the localized impulsive energy release in the solar chromosphere. It should be noted that the present simulations are essentially two-dimensional. This leads to a different redistribution of kinetic energy in the numerical domain, if compared to the more realistic three-dimensional scenario. In 2D case the energy will be guided in the vertical direction as there is one less horizontal direction for the energy to spread. It leads underestimation of the energy required to generate such a jet, therefore, may put an overestimate of the jet height. Therefore, a significantly larger velocity amplitude may be required in 3-D simulations to generate the jet than what is seen in the observations. However, our chapter will serve as a ready reference for the forthcoming more realistic 3-D simulations that will further explore the triggering mechanisms of such spicule-like jets in greater details. We admit the inherent limitations (e.g., 2-D scenario, focus on single fluid MHD only, simple magnetic field configurations), however, the present chapter consists of a potential scientific idea as already delineated. This physical aspect of the jet formation must be taken in greater details further using more

sophisticated observations and realistic modeling. The new generation telescopes and their back-end instruments (e.g., DKIST, IRIS, SST, etc) may be shedding more new lights on the impulsive origin of the cool jets and the effect of energy imbalance conditions on them. This particular effort will further allow modelers to put forward new refined models vis-á-vis high-resolution observations in the coming future.

In the next Chapter 6, we describe the numerical model about the formation of spicule-like cool jets under the effect of multiple vertical velocity pulses. We also study the properties of transverse kink oscillations evolved in two model jets.